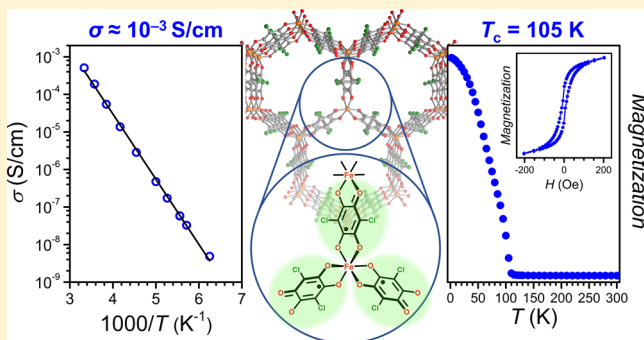


2D Conductive Iron-Quinoid Magnets Ordering up to $T_c = 105$ K via Heterogenous Redox ChemistryJordan A. DeGayner,[†] Je-Rang Jeon,[†] Lei Sun,[‡] Mircea Dincă,[‡] and T. David Harris^{*,†}[†]Department of Chemistry, Northwestern University, Evanston, Illinois 60208-3313, United States[‡]Department of Chemistry, Massachusetts Institute of Technology, Cambridge, Massachusetts 02139-4307, United States

S Supporting Information

ABSTRACT: We report the magnetism and conductivity for a redox pair of iron-quinoid metal–organic frameworks (MOFs). The oxidized compound, $(\text{Me}_2\text{NH}_2)_2[\text{Fe}_2\text{L}_3] \cdot 2\text{H}_2\text{O} \cdot 6\text{DMF}$ ($\text{LH}_2 = 2,5\text{-dichloro-3,6-dihydroxy-1,4-benzoquinone}$) was previously shown to magnetically order below 80 K in its solvated form, with the ordering temperature decreasing to 26 K upon desolvation. Here, we demonstrate this compound to exhibit electrical conductivity values up to $\sigma = 1.4(7) \times 10^{-2}$ S/cm ($E_a = 0.26(1)$ eV) and $1.0(3) \times 10^{-3}$ S/cm ($E_a = 0.19(1)$ eV) in its solvated and desolvated forms, respectively. Upon soaking in a DMF solution of Cp_2Co , the compound undergoes a single-crystal-to-single-crystal one-electron reduction to give $(\text{Cp}_2\text{Co})_{1.43}(\text{Me}_2\text{NH}_2)_{1.57}[\text{Fe}_2\text{L}_3] \cdot 4.9\text{DMF}$. Structural and spectroscopic analysis confirms this reduction to be ligand-based, and as such the trianionic framework is formulated as $[\text{Fe}^{\text{III}}_2(\text{L}^{3-\bullet})_3]^{3-}$. Magnetic measurements for this reduced compound reveal the presence of dominant intralayer metal–organic radical coupling to give a magnetically ordered phase below $T_c = 105$ K, one of the highest reported ordering temperatures for a MOF. This high ordering temperature is significantly increased relative to the oxidized compound, and stems from the overall increase in coupling strength afforded by an additional organic radical. In line with the high critical temperature, the new MOF exhibits magnetic hysteresis up to 100 K, as revealed by variable-field measurements. Finally, this compound is electrically conductive, with values up to $\sigma = 5.1(3) \times 10^{-4}$ S/cm with $E_a = 0.34(1)$ eV. Taken together, these results demonstrate the unique ability of metal-quinoid MOFs to simultaneously exhibit both high magnetic ordering temperatures and high electrical conductivity.



■ INTRODUCTION

The simultaneous implementation of high-temperature magnetic order and high electrical conductivity within a single material represents a formidable challenge in the synthesis of multifunctional materials for next-generation data processing and storage.^{1,2} Specifically, conductive magnets are of considerable interest for spintronics applications, where electronic spin ensembles are manipulated through electrical and magnetic fields to perform logic operations and store information.³ Materials employed in spintronics applications historically comprise inorganic solids where direct metal–metal bonding or short mono- or diatomic ligands enable the efficient long-range electronic communication essential to both magnetic order and electrical conductivity.⁴ Despite the success of these materials, their all-inorganic compositions greatly limit their directed synthesis and chemical tunability.

In contrast, metal–organic frameworks (MOFs) constitute a class of materials that have garnered tremendous attention owing largely to their synthetic programmability and tunability in conjunction with their structural porosity. Through careful control of synthetic conditions, the physical and chemical properties of MOFs can be targeted and optimized through

systematic tuning of the organic linker, metal node, and framework topology.^{5,6} Furthermore, the presence of structural pores can allow facile postsynthetic modification through diffusion of reactants that are incompatible with conventional solution-based synthesis conditions, thereby enabling the fine-tuning of properties through techniques such as guest molecule inclusion, redox chemistry, and covalent modification.^{7–10}

A central challenge in the design of conductive metal–organic magnets is that both magnetic ordering and electrical conductivity rely on the presence of efficient electronic communication between structural units. Indeed, this scenario is at direct odds with typical MOF compositions, which predominantly involve ionic bonding between closed-shell metal ions and large, redox-inert organic linkers.⁵ Consequently, this trade-off usually results in either porous materials with no long-range electronic communication or materials with strong coupling but negligible porosity. To illustrate, to date there is no reported example of a material with a reported Brunauer–Emmett–Teller (BET) surface area greater than

Received: January 20, 2017

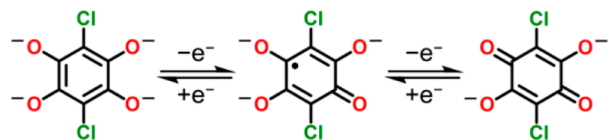
Published: February 23, 2017

1000 m²/g that exhibits either long-range magnetic order above 10 K or conductivity above 10^{−6} S/cm.^{11,12} Moreover, to the best of our knowledge, the literature contains only three examples of structurally characterized metal–organic solids that magnetically order at or above 100 K.^{13–15}

One strategy to surmount this challenge centers on the construction of hybrid materials that are composed of separate magnetic and conductive components;⁷ however, this methodology is likely to result in materials that possess diluted properties associated with their constituents rather than new materials with emergent properties that are greater than the sum of their parts. As an alternative, one can envision the use of redox-active bridging ligands as linkers between paramagnetic, redox-active metal nodes. This approach allows in situ or postsynthetic redox reactions to generate an organic radical on the bridging ligand.¹⁶ Here, the presence of linkers that bear radical character gives rise to strong, direct exchange interactions between the metal nodes and ligands, thereby promoting magnetic order at high temperatures. Toward electrical conduction, redox-active ligands promote charge transfer, and the presence of an organic radical provides a high-energy electron or hole for a charge hopping mechanism. Indeed, to date this approach has yielded the first molecule-based material that exhibits magnetic order above room temperature¹⁷ and the highest electrical conductivity observed in a permanently porous MOF.^{18,19}

Benzoquinoid ligands are bis-bidentate ligands that can readily access three oxidation states (see Scheme 1) and have

Scheme 1. Redox Series of Deprotonated Benzoquinoid Linkers Based on Chloranilic Acid: Left to Right, L^{4−}, L^{3−•}, L^{2−}



been shown to form porous networks.^{20,21} Chemical reduction from the dianionic benzoquinone to the trianionic semiquinone results in the generation of a delocalized organic radical with significant spin density on the donor atoms.²² When bound to paramagnetic metal centers, this allows for a strong direct-exchange magnetic coupling mechanism due to a largely covalent interaction between metal and ligand. As such, 2,5-dihydroxy-1,4-benzoquinone and its many derivatives are effective paramagnetic linkers in dinuclear systems,²³ while tetraoxolene radicals have recently generated extended solids that exhibit strong magnetic coupling.^{24–26}

We recently reported the discovery of long-range magnetic order in a two-dimensional (2D) honeycomb solid comprised of Fe^{III} centers bridged by chloranilate radical ligands. Magnetic measurements of this solid revealed spontaneous magnetization below 80 K. Furthermore, desolvation to generate the activated material resulted in a reduction in the ordering temperature to 26 K with a measured BET surface area of 885(105) m²/g.²⁴ Herein, we report the observation of high electrical conductivity in both the solvated and activated material. An improvement in the activation protocol leads to an increase in the measured BET surface area to 1175(29) m²/g, which to our knowledge represents the highest surface area yet observed for a magnet or conductive material. Furthermore, the porosity of

the solid enables postsynthetic single-crystal-to-single-crystal chemical reduction of the framework to give a magnetically ordered phase with a critical temperature of *T*_c = 105 K, providing an extremely rare example of a structurally characterized metal–organic solid that magnetically orders above 100 K.

EXPERIMENTAL SECTION

General Considerations. The manipulations described below were performed under a dinitrogen atmosphere in an MBraun LABstar glovebox, operated under a humid atmosphere, or in a Vacuum Atmospheres Nexus II glovebox. Dimethylformamide (DMF), tetrahydrofuran (THF), and benzene were dried using a commercial solvent purification system from Pure Process Technology, and THF and benzene were stored over 4 Å molecular sieves prior to use. Effective removal of oxygen and moisture in THF and benzene was verified using a standard purple solution of sodium benzophenone ketyl. The compounds (Me₂NH₂)₂[Fe₂L₃]·2H₂O·6DMF (**1**) and (Me₂NH₂)₂[Zn₂L₃]·2H₂O·6DMF (**3**) were prepared as previously described.²⁴ All reagents were purchased from commercial vendors and used without further purification.

(Me₂NH₂)₂[Fe₂L₃] (**1a**). The desolvated form of this compound was generated by soaking a crystalline sample of **1** (180 mg, 0.139 mmol) in THF (10 × 10 mL) for 3 days followed by further soaking in benzene (10 × 10 mL) for 3 days. The final benzene wash was then removed through sublimation at reduced pressure at −78 °C for 36 h. The material was further activated by heating for 24 h at 120 °C under reduced pressure to yield **1a** (95.5 mg, 83%). FT-IR (ATR, cm^{−1}): 3121(w, br); 2805(w); 1655(w); 1482(s); 1363(s); 1283(m); 1212(m); 1000(m); 852(s); 767(m); 576(m); 485(s); 412(m). Anal. Calcd for C₂₂H₁₆Fe₂N₂O₁₂Cl₆: C 32.0, H 1.96, N 3.40%. Found: C, 31.8; H, 2.19; N, 3.64%.

(Cp₂Co)_{1.43}(Me₂NH₂)_{1.57}[Fe₂L₃]·4.9DMF (**2**). This compound was prepared by soaking crystals of **1** (203 mg, 0.156 mmol) in a solution of cobaltocene (118 mg, 0.624 mmol) in DMF (6 mL) at ambient temperature for 48 h. The supernatant was decanted and the solid washed with DMF (10 × 10 mL) over 3 days and collected by filtration to yield **2** (0.198 g, 88%). FT-IR (ATR, cm^{−1}): 3075 (w, br); 2926 (w); 2852 (w); 2773 (w, br); 2471 (w, br); 1647 (s); 1474(s); 1413(s); 1374(s); 1279(m); 1088(m); 1028(m); 845(s); 662(m); 573 (m); 479 (s); 421 (m). Anal. Calcd for C_{50.17}H_{61.17}Fe₂Co_{1.43}N_{6.47}O_{16.9}Cl₆: C 41.4, H 4.30, N 6.32%. Found: C, 42.0; H, 4.45; N, 6.22%. Molar metal ratio from ICP-OES analysis: Fe:Co = 1.99:1.43.

X-ray Structure Determination. Single crystals of **2** suitable for X-ray analysis were coated with deoxygenated Paratone-N oil and mounted on a MicroMounts rod. The crystallographic data were collected at 100 K on a Bruker APEX II diffractometer equipped with a Cu Kα microsource. Raw data were integrated and corrected for Lorentz and polarization effects using Bruker APEX2 v. 2009.1,²⁷ and absorption corrections were applied using SADABS.²⁸ The space group assignment was determined by examination of systematic absences, E-statistics, and successive refinement of the structure. The structure was solved and refined with SHELXL²⁹ operated with the OLEX2 interface.³⁰ A cobaltocenium ion and solvent molecules were severely disordered and could not be modeled properly. Therefore, the solvent masking procedure as implemented in OLEX2 was used. A total of 80.6 electrons per unit-cell were estimated and ascribed to the combination of a cobaltocenium ion and disordered DMF solvent molecules. Due to this disorder and the general poor quality of the single-crystal X-ray diffraction data, the chemical formula is based on elemental analysis from C, H, and N combustion and ICP-OES. Hydrogen atoms for the dimethylammonium ions were placed at calculated positions using suitable riding models and refined using isotropic displacement parameters derived from their parent atoms. Thermal parameters were refined anisotropically for all non-hydrogen atoms. Crystallographic data and the details of data collection are listed in Table 1.

Table 1. Crystallographic Data for 2

empirical formula	C _{50.1} H _{61.2} Cl ₆ Fe ₂ Co _{1.43} N _{6.5} O _{16.9}
formula weight, g/mol	1433.6
crystal system	trigonal
space group	<i>P</i> 3̄1 <i>m</i>
wavelength, Å	1.54178
temp, K	100
<i>a</i> , Å	13.584(1)
<i>b</i> , Å	13.584(1)
<i>c</i> , Å	8.680(1)
α , deg	90
β , deg	90
γ , deg	120
<i>V</i> , Å ³	1386.9(3)
<i>d</i> _{calc} , g/cm ³	1.034
<i>R</i> ₁ (<i>I</i> > 2σ(<i>I</i>)) ^a	0.1222
<i>wR</i> ₂ (all) ^b	0.3189
GoF	1.105

^a*R*₁ = Σ||*F*₀| − |*F*_C||/Σ|*F*₀|. ^b*wR*₂ = [Σ*w*(*F*₀² − *F*_C²)/Σ*w*(*F*₀²)]^{1/2}.

Powder X-ray Diffraction Analyses. A powder sample of **1** was sandwiched between two pieces Kapton tape in the 3 mm hole of a metallic mask in a dinitrogen glovebox. Powders of **1a** and **2** were transferred to a boron-rich capillary tube with 1.0 mm (**1a**) or 0.7 mm (**2**) outer diameter in a nitrogen-filled glovebox. The tubes were capped with a septum, evacuated on a Schlenk line outside of the glovebox while immersed in liquid nitrogen, and flame-sealed. Powder X-ray diffraction data for **1** and **1a** were collected at ambient temperature on a STOE-STADIMP powder diffractometer equipped with an asymmetric curved Germanium monochromator (Cu Kα1 radiation, λ = 1.54056 Å) and one-dimensional silicon strip detector (MYTHEN2 1K from DECTRIS), and the sample was measured in transmission (**1**) or Debye–Scherrer (**1a**) geometry in a rotating holder. The line focused Cu X-ray tube was operated at 40 kV and 40 mA. Intensity data from 5 to 50 degrees two theta were collected over a period of 20 min. The instrument was calibrated against a NIST Silicon standard (640d). For **2**, high resolution synchrotron powder diffraction data were collected using beamline 11-BM at the Advanced Photon Source of Argonne National Laboratory using an average wavelength of 0.414617 Å. Discrete detectors covering an angular range from −6 to 16 degrees two theta were scanned over a 34 degree two theta range, with data points collected every 0.001 degrees 2θ and scan speed of 0.01 deg/s. These data are provided in Figure S1.

Nitrogen Adsorption Measurements. Crystalline **1a** was transferred to a tared analysis tube under an atmosphere of nitrogen and capped with a Transeal fitting. The sample was then transferred to a Micrometrics ASAP 2020 gas adsorption analyzer and heated at a rate of 5 K/min from ambient temperature to 393 K under dynamic vacuum. Activation was continued for 24 h until an outgas rate of less than 1 mTorr/min was observed. The evacuated tube containing the activated sample was then transferred to a balance and weighed to determine the mass of the sample. The tube was transferred then to the analysis port of the instrument, where the outgas rate was again determined to be less than 1 mTorr/min. Nitrogen uptake was measured using volumetric methods, and the free space of the sample was determined with UHP He prior to analysis. The N₂ adsorption isotherm at 77 K was measured in liquid nitrogen. The reported surface area value of 1175(30) m²/g was averaged from independent measurements performed on 2 different samples (see Figure S2).

Magnetic Measurements. Magnetic measurements of **1** and **2** were performed on polycrystalline samples sealed in a polyethylene bag under a dinitrogen atmosphere. All data were collected using a Quantum Design MPMS-XL SQUID magnetometer from 1.8 to 300 K at applied dc fields ranging from 0 to +7 T. Ac magnetic susceptibility data were collected under an ac field of 4 Oe, oscillating at frequencies in the range 1–1488 Hz. Dc susceptibility data were corrected for diamagnetic contributions from the sample holder and

for the core diamagnetism of each sample (estimated using Pascal's constants³¹). The coherence of the collected data was confirmed across different measurements. The magnetic ordering temperatures for **1a** and **2** were determined by the peak of χ_M' as plotted versus temperature.

Raman Measurements. Crystals of **1**, **1a**, and **2** were deposited onto a silicon oxide-coated silicon wafer and sealed in a Linkam THMS350 V microscope state. Raman spectra were collected using a Horiba LabRam HR Evolution confocal microscope. Individual crystals were excited with a 473 nm continuous-wave diode laser (Cobalt Blue) at 263 μW power equipped with a long working distance 50× microscope objective (NA = 0.50; Nikon) and 1800 grooves/mm grating. Spectra were collected for **6**, **2**, and 4 min for **1**, **1a**, and **2**, respectively. Data for **1a** are shown in Figure S3. Data for **3** correspond to those reported in ref 24.

Electrical Conductivity Measurements. Two-point dc conductivity data were collected in a dinitrogen-filled glovebox at 300 K using a home-built press and a Keithley 6517B electrometer, as previously described.³² The powder was pressed between two steel rods of 2 mm diameter inside of a glass capillary. The thickness of the pressed pellets typically ranged from 0.1 to 0.5 mm. Variable-temperature dc conductivity data were collected between 110 and 300 K with a home-built two-screw press²⁵ and a Keithley 6517B (**1**, **1a**) or CHI 760c (**2**) electrometer. The powder was pressed between two stainless steel screws inside of a plastic tube made of Garolite 10. For **1** and **1a**, the pressed pellets were prepared in a dinitrogen-filled glovebox, transferred into a Janis probe station (ST-500) through a miniature vacuum transfer chamber, and kept in a dark environment and under vacuum (ca. 10^{−5} Torr). For **2**, the Garolite cell was attached to a SQUID sample rod using silver epoxy and then lowered into the cryostat-equipped SQUID chamber, where data were collected using a CHI 760c electrometer.

Other Physical Measurements. Elemental analyses of **1**, **1a**, and **2** were performed by the Midwest Microlab (Indianapolis, IN). Infrared spectra were recorded in a nitrogen-filled glovebox on a Bruker Alpha FTIR spectrometer equipped with an attenuated total reflectance accessory (see Figure S4). Zero-field iron-57 Mössbauer spectra for **2** was obtained at 80 and 120 K with a constant acceleration spectrometer and a cobalt-57 rhodium source. Prior to the measurements, the spectrometer was calibrated at 295 K with α-iron foil. Samples were prepared in a dinitrogen-filled glovebox, covered with deoxygenated Paratone-N oil, and frozen in liquid nitrogen prior to handling in air. The sample of **2** contained approximately 4 mg/cm² of iron. The spectra were analyzed using the WMOSS Mössbauer Spectral Analysis Software (www.wmoss.org).

RESULTS AND DISCUSSION

Syntheses and Structures. The solvated hexagonal framework compound (Me₂NH₂)₂[Fe₂L₃]·2H₂O·6DMF (**1**) was synthesized as previously described.²⁴ Its activation was carried out in an improved procedure whereby successive soaks in THF and benzene, followed by lyophilization at −78 °C and evacuation at 120 °C, gave the desolvated compound [Me₂NH₂]₂[Fe₂L₃] (**1a**). This new activation procedure led to an increase in the BET surface area from the previously reported 885(105) m²/g²⁴ to 1175(29) m²/g, likely due to a better preservation of the solid-state structure owing to lyophilization of benzene prior to heating. Indeed, similar lyophilization-based methods have previously been shown to increase the observed surface area in MOFs prone to structural collapse. This effect has been attributed to a reduction in capillary forces generated from sublimation of the frozen solvent compared to evaporation of the liquid solvent.³³

The porous structure of **1** offers the possibility to carry out postsynthetic redox chemistry. Toward this end, single crystals of **1** were allowed to stand in a DMF solution of excess Cp₂Co for 48 h. Subsequent washing with DMF gave the reduced

compound $(\text{Cp}_2\text{Co})_{1.43}(\text{Me}_2\text{NH}_2)_{1.57}[\text{Fe}_2\text{L}_3]\cdot 4.9\text{DMF}$ (**2**) as black crystals. Quantitative one-electron reduction of the framework was monitored and confirmed by a combination of vibrational spectroscopy, ICP-OES trace metals analysis, and C, H, and N combustion analysis (see below and [Experimental Section](#)). Attempts to desolvate **2** have thus far led to loss of crystallinity and porosity.

Remarkably, single-crystal X-ray analysis revealed the preservation of single crystallinity upon reduction of **1** to **2**. Single-crystal to single-crystal redox transformations in metal–organic frameworks have been observed in a handful of instances but are still a relatively rare phenomenon.³⁴ This ability to perform postsynthetic redox chemistry without framework disruption highlights the utility of high porosity in multifunctional materials and enables detailed structural comparison before and after reduction.

Similar to that of **1**, the structure of **2** consists of 2D honeycomb-like layers that stack in a perfectly eclipsed arrangement along the crystallographic *c* axis (see [Figure 1](#)).

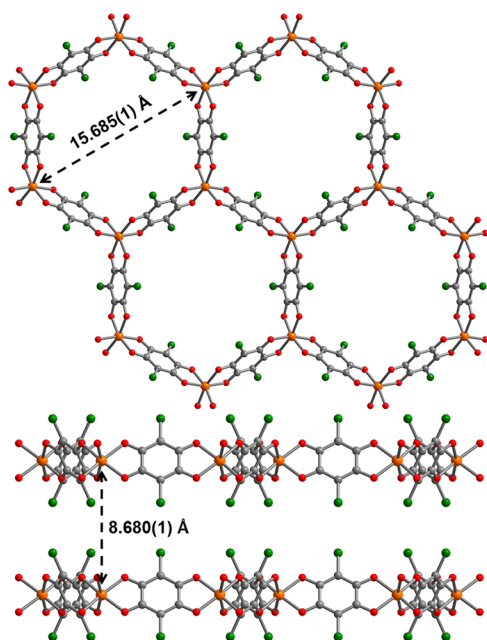


Figure 1. X-ray crystal structure of $[\text{Fe}_2\text{L}_3]^{3-}$, as observed in **2**, viewed along the crystallographic *c* axis (upper) and *b* axis (lower) with selected $\text{Fe}\cdots\text{Fe}$ distances. Orange, green, red, and gray spheres represent Fe, Cl, O, and C atoms, respectively; cations and DMF molecules are omitted for clarity.

This eclipsed stacking pattern gives rise to one-dimensional channels that feature an average intralayer, cross-channel $\text{Fe}\cdots\text{Fe}$ distance of 15.685(1) Å, similar to that of 15.6614(6) Å previously reported for **1**.²⁴ Each layer comprises Fe centers coordinated to three $\text{L}^{3-\bullet}$ ligands to form an octahedral coordination sphere. A crystallographically imposed 3-fold rotation axis at each Fe site renders all ligands structurally equivalent. Along the *c* axis, adjacent layers feature a closest $\text{Fe}\cdots\text{Fe}$ distance of 8.680(1) Å, which represents a 0.7% decrease relative to **1**. This smaller interlayer spacing for **2** may largely result from increased ionic interactions between the anionic layers and interstitial cations.

The overall trianionic charge of the reduced framework $[\text{Fe}_2\text{L}_3]^{3-}$ in **2** is partially compensated by $(\text{Me}_2\text{NH}_2)^+$ cations generated from DMF decomposition during the synthesis of

1.³⁵ In addition, ICP-OES analysis revealed the remainder of charge compensation to be provided by $[\text{Cp}_2\text{Co}]^+$ cations, however these cations cannot be appropriately modeled in the crystal structure owing to severe disorder (see [Experimental Section](#)). Nevertheless, examination of the structure reveals large, solvent-accessible voids both in the hexagonal channels and in the interlayer space that could accommodate a $[\text{Cp}_2\text{Co}]^+$ cation. In addition, a combination of ICP-OES and C, H, and N combustion elemental analysis showed the presence of partial substitution of excess $[\text{Cp}_2\text{Co}]^+$ for $(\text{Me}_2\text{NH}_2)^+$. The precise extent of cation exchange was found to vary slightly across multiple reactions, typically resulting in 1.3–1.5 $[\text{Cp}_2\text{Co}]^+$ and 1.7–1.5 $(\text{Me}_2\text{NH}_2)^+$ cations per unit cell, respectively. Note that all analysis reported herein corresponds to a single formulation of 1.43 (Cp_2Co) : 1.57 (Me_2NH_2) ; differences in magnetism and conductivity across samples with slightly different cation formulations were found to be insignificant.

Whereas the 2D topologies in **1**, **2**, and **3** are very similar, an examination of framework bond distances in these compounds reveals several subtle differences. First, upon reduction of **1** to **2**, the mean $\text{Fe}-\text{O}$ bond distance increases slightly from 2.020(4) to 2.028(5) Å, although these values fall within error of one another. In both compounds, this distance can be unambiguously assigned to high-spin Fe^{III} .^{24,36} Within the bridging ligand, the mean $\text{C}-\text{C}$ bond distance in **1** is 1.6% shorter than that in **3**, while the $\text{C}-\text{O}$ distance is 2.9% longer in **1**.²⁴ This observation is consistent with the presence of exclusively L^{2-} in **3**, which is therefore formulated to contain $[\text{Zn}^{\text{II}}_2(\text{L}^{2-})_3]^{2-}$, and an average of one L^{2-} and two $\text{L}^{3-\bullet}$ in **1**, formulated as $[\text{Fe}^{\text{III}}_2(\text{L}^{2-})(\text{L}^{3-\bullet})_2]^{2-}$. Further, the two organic radicals in **1** were previously shown, through an array of structural and spectroscopic analysis, to be delocalized over every three ligands to give a composition of $[\text{Fe}^{\text{III}}_2(\text{L}_3^{8-})]^{2-}$.²⁴ In other words, each ligand in **1** can be viewed as accommodating two-thirds of an unpaired electron.

Compound **1** features a $\text{C}-\text{O}$ bond distance of 1.280(5) Å, slightly shorter than the corresponding distance of 1.30(1) Å observed in **2**. In contrast, whereas the mean $\text{C}-\text{C}$ bond distances in **1** and **2** also fall within error of one another, the $\text{C1}-\text{C1A}$ bond distance undergoes a statistically significant contraction from 1.480(9) Å to 1.43(2) Å in moving from **1** to **2** (see [Figure 2](#)). Indeed, this $\text{C}-\text{C}$ bond distance has been shown to serve as a reliable indicator of benzoquinoid oxidation state in related molecular species, where it shortens upon reduction.²³ These observations, in conjunction with the statistically identical $\text{Fe}-\text{O}$ bond distances in the two compounds, suggests a ligand-centered reduction in moving from **1** to **2**. Accordingly, the framework composition in **2** can be best described as $[\text{Fe}^{\text{III}}_2(\text{L}^{3-\bullet})_3]^{3-}$, where each semiquinoid bridging ligand now hosts a full unpaired electron. Nevertheless, this assignment should not be regarded as conclusive from X-ray diffraction analysis alone, given the nearly identical bond distances in **1** and **2**. Note, however, that a net one-electron ligand-centered reduction in moving from **1** to **2** corresponds to addition of only one-third of an electron per ligand, and as such large changes to bond distances are not expected to accompany the reaction.

Raman Spectroscopy. To further assess the bridging ligand oxidation state in each compound, Raman spectra were compared for solid samples of **1**, **2**, and **3** at ambient temperature using an excitation wavelength of 473 nm (see [Figure 3](#)). The bands observed at 1491, 1487, 1617 cm^{-1} for **1**–**3**, respectively, are assigned to the $\text{C}-\text{O}$ stretching mode of

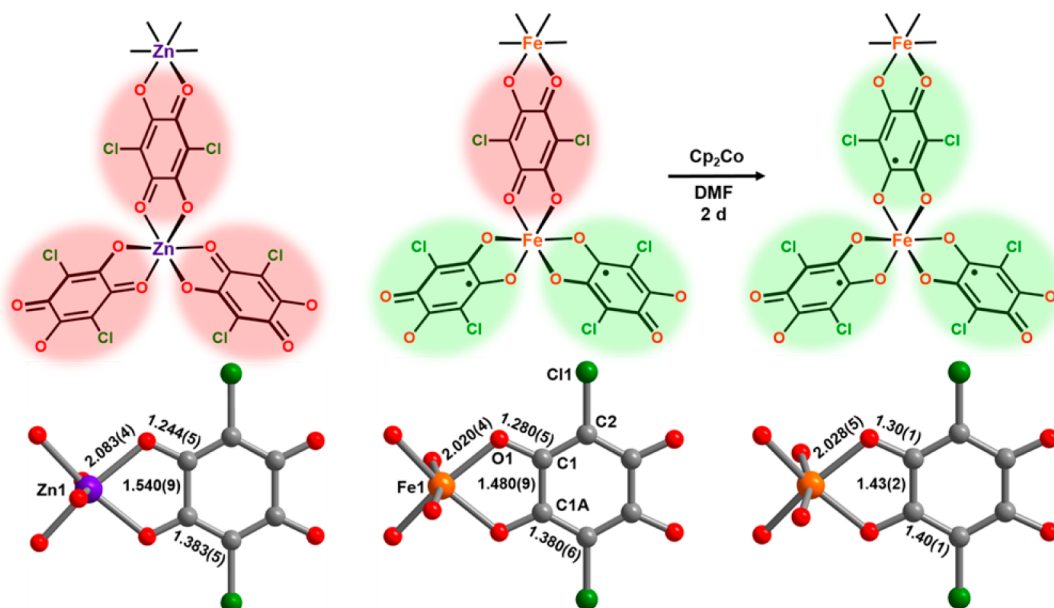


Figure 2. Upper: Scheme depicting the repeating unit of the 2D frameworks in 3, 1, and 2 (left to right), highlighting the oxidation state of the bridging ligand. Lower: Portions of crystal structures for 3, 1, and 2, highlighting relevant bond distances (Å).

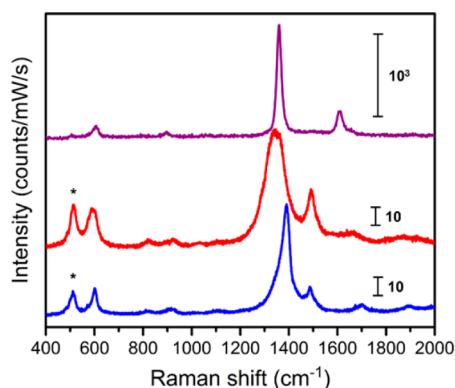


Figure 3. Raman spectra collected for solid samples of 1 (red), 2 (blue), and 3 (purple), following excitation at 473 nm (1 and 2) or 405 nm (3). The peaks marked with an asterisk are assigned to the Si support.

the bridging ligand. In agreement with X-ray diffraction analysis, the frequency observed for 3 can be ascribed to L²⁻. In contrast, the much lower frequency for 1 compared to 3 is assigned to the two-electron reduction per three bridging ligands in 1, as described above.^{22,24,37} Upon moving from 1 to 2, this band is further shifted to lower frequency, albeit to a much lower degree. This decrease in frequency is consistent with a ligand-based reduction upon moving from 1 to 2, and the small magnitude of the shift is consistent with the corresponding small change in C–O bond distance obtained from single-crystal X-ray diffraction analysis.

The Raman bands at 1364, 1390, and 1360 cm⁻¹ for 1–3, respectively, are assigned to the C–C stretching mode within the bridging ligand ring. In stark contrast to the subtle shift in C–O frequency, the C–C bond becomes considerably stronger upon reduction from 1 to 2. This observation illustrates a net increase in bond order upon reduction, in line both with the shortening of the C1–C1A bond distance and with previous reports of semiquinoid radicals.^{38,39} Finally, the features at 594 and 601 cm⁻¹ for 1 and 2 are tentatively assigned to CC-

coupled Fe–O stretching modes.^{38,39} Here, the higher frequency observed for the former compound is likely reflective of a slightly stronger Fe–O bond engendered by a more negatively charged ligand field. Taken together, the shifts in the C–O, C–C, and Fe–O vibrational frequencies further support the assignment of a ligand-based reduction from [Fe^{III}₂(L⁸⁻)₃]²⁻ in 1 to [Fe^{III}₂(L^{3-•})₃]³⁻ in 2.

In addition to enabling assignment of ligand oxidation state in 1–3, the comparison of Raman spectra for the three compounds reveals a trend that is perhaps reflective of ligand electronic structure.²⁴ Upon moving from 3, which features exclusively L²⁻, to 1, which features formally 2:1 L^{3-•}:L²⁻, the energy of the C–C stretching mode remains relatively constant, increasing by only 4 cm⁻¹, while the C–O vibration undergoes a dramatic shift to lower energy of ca. 140 cm⁻¹. In contrast, upon moving from 1 to 2, which features exclusively L^{3-•}, the opposite trend is observed. Here, the C–O vibration undergoes only a modest shift of 4 cm⁻¹, while the C–C vibration increases in energy by 26 cm⁻¹. This incongruent dependence of vibrational frequencies on ligand oxidation state likely results from populating different ligand-based orbitals. For instance, the data suggest that the additional two electrons in 1 relative to 3 are added to an orbital of primarily C–O π* character. In contrast, the data suggest that upon reduction of 1 to 2, the additional electron resides in an orbital of primarily π character centered on the C1–C1A bond.

Mössbauer Spectroscopy. To confirm the preservation of the Fe^{III} oxidation state upon reduction from 1 to 2, Mössbauer spectra were collected for a solid sample of 2. The spectrum at 80 K exhibits a broad, poorly resolved sextet that indicates the onset of magnetic ordering (see Figure S5).⁴⁰ Qualitatively, this observation shows that 2 undergoes magnetic ordering at a higher temperature than does 1, which shows no evidence of a sextet at 80 K. Upon increasing the temperature to 120 K, the spectrum for 2 resolves into a sharp quadrupole doublet that can be fit to an isomer shift of $\delta = 0.541(1)$ mm/s and a quadrupole splitting of $\Delta E_Q = 1.018(3)$ mm/s (see Figure 4), with a miniscule amount of high-spin Fe^{II} impurity. These

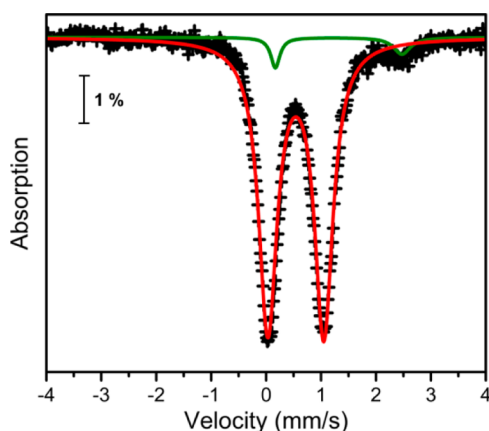


Figure 4. Mössbauer spectrum collected for a crystalline sample of **2** at 120 K. Black crosses represent experimental data, and solid lines correspond to fits to the data.

parameters can be unambiguously assigned to a high-spin Fe^{III} center, thereby confirming the one-electron reduction from **1** to **2** to be ligand-centered.⁴¹ Moreover, these values are similar, albeit slightly different, than those of $\delta = 0.576(1)$ and $\Delta E_Q = 1.059(2)$ mm/s previously reported for **1** at 80 K. The slightly smaller isomer shift observed in **2** is likely due to an increase in electron density on the Fe^{III} center upon ligand reduction and/or a slight temperature dependence of the spectra.

Magnetic Properties. In order to probe the magnetic behavior of **1a** and **2**, variable-temperature dc magnetic susceptibility data were collected. The resulting plots of $\chi_M T$ vs T are shown in Figures S6 and S7. Even with the increase in surface area of **1a** upon subjecting **1** to the new activation procedure, the magnetic properties of **1a** were found to be similar to those previously reported for the desolvated compound (see Figures S8 and S9).²⁴ For **2**, at 300 K under an applied dc field of 10 Oe, the value of $\chi_M T = 26.5 \text{ cm}^3 \text{ K mol}^{-1}$ is considerably larger than that of $9.875 \text{ cm}^3 \text{ K mol}^{-1}$ expected for two Fe^{III} centers and three $\text{L}^{3-\bullet}$ ligands that are magnetically isolated from one another. This observation indicates some degree of long-range magnetic interactions between paramagnetic centers. Moreover, the value of $26.5 \text{ cm}^3 \text{ K mol}^{-1}$ is considerably higher than that of $16.6 \text{ cm}^3 \text{ K mol}^{-1}$ previously reported for **1**. This difference likely implies an overall stronger collection of coupling pathways in **2** compared to **1**, although basing such an assertion on these high-temperature data is tentative given the slightly different number of unpaired electrons in the two compounds. As the temperature decreases, the value of $\chi_M T$ increases only gradually until 115 K, where a sharp increase is observed. The value of $\chi_M T$ then reaches a maximum at 60 K before decreasing again. This behavior stems from the growth of magnetically correlated domains with decreasing temperature under an applied field, indicating the onset of magnetic order. Furthermore, comparison of dc magnetization and magnetic susceptibility plots collected upon cooling the sample with and without an externally applied dc field reveals a divergence of the magnetization at 105 K, further supporting the observation of spontaneous magnetization (see Figures 5, S10, and S11).

To investigate the presence of magnetic hysteresis and nature of coupling interactions in **2**, variable-field magnetization data were collected at selected temperatures. Remarkably, compound **2** exhibits an open hysteresis loop up to 100 K under a field-sweep rate of 0.05 Oe/s (see Figure 6). Furthermore,

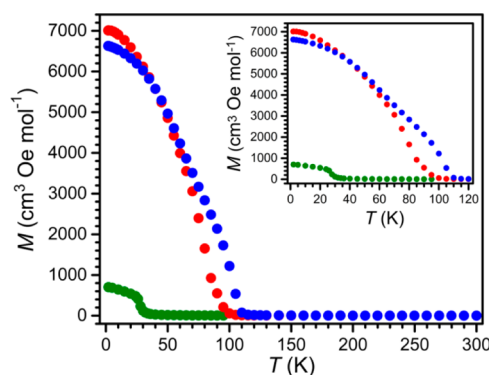


Figure 5. Variable-temperature field-cooled magnetization data for **1** (red), **1a** (green), and **2** (blue), collected under an applied dc field of 10 Oe.

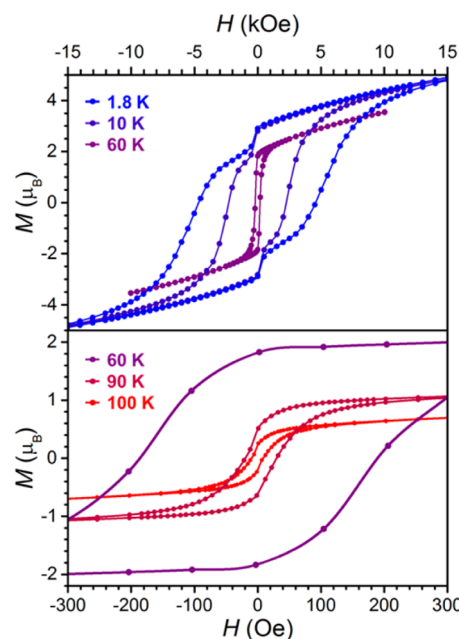


Figure 6. Variable-field magnetization data for **2** collected at selected temperatures.

examination of plots of magnetization versus applied field provides intrinsic coercive fields of $H_{\text{ci}} = 4520, 2270, 186, 25$, and 9 Oe at 1.8, 10, 60, 90, and 100 K, respectively, with field-sweep rates of 4.5, 4.4, 0.9, 0.09, and 0.05 Oe/s. The intrinsic coercivity for **2** at 1.8 K is nearly twice that reported for **1** and is similar to that reported for **1a**. Although this difference is likely best attributed to an increase in magnetic anisotropy in moving from **1** to **2**, a detailed understanding of this comparison is not immediately forthcoming. Finally, at 60 K, **2** exhibits an intrinsic coercivity that is an order of magnitude larger than that reported for **1**. In all three compounds, steps in the low temperature magnetic hysteresis are observed near zero-field. While the exact nature of this feature is currently unknown, it likely reflects the magnetic anisotropy of the sample due to the strong intralayer and relatively weak interlayer interactions.

At 1.8 K, the data reach a maximum value of $M = 6.0 \mu_B$ at 50 kOe (see Figure 6), near the value of $7 \mu_B$ predicted for an overall $S = 7/2$ repeating unit stemming from two $S = 5/2$ Fe^{III} centers antiferromagnetically coupled to three $S = 1/2$ $\text{L}^{3-\bullet}$ radical ligands. This magnetization value is smaller than the maximum of $8.2 \mu_B$ reported for **1** at 70 kOe, consistent with

the larger repeating unit of $S = 4$ in **1**. These data strongly suggest that the magnetic behavior in **2** is dominated by intralayer metal–organic radical coupling, such that **2** is likely best described as a 2D bulk ferrimagnet. Note, however, that the present analysis of magnetic behavior alone cannot definitively determine the order of dimensionality, and as such the characterization of **2** as a 2D ferrimagnet should be considered as tentative.

To precisely determine the magnetic ordering temperature of **2**, variable-temperature ac magnetic susceptibility measurements were collected at selected frequencies under zero applied dc field. The data reveal a frequency-independent peak in both the in-phase (χ_M') and out-of-phase (χ_M'') susceptibility plots at 105 K, indicative of a critical magnetic ordering temperature of $T_c = 105$ K (see Figure 7). This value of T_c represents an

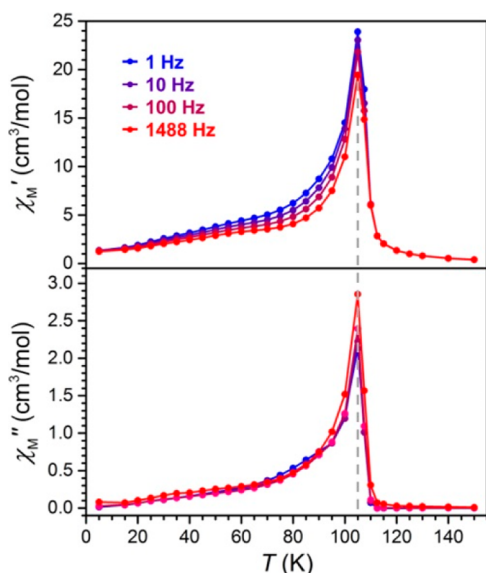


Figure 7. Variable-temperature ac susceptibility data for **2**, collected under zero dc field at selected frequencies. The gray dashed vertical line serves as a guide to the eye and denotes an ordering temperature of $T_c = 105$ K.

increase of 25 K, or 31%, over that reported for **1**. Indeed, the observation of an increase despite a net decrease in overall spin magnitude most likely reflects an overall strengthening of magnetic coupling interactions associated with moving from a net two-thirds unpaired electron to a full unpaired electron residing on each bridging ligand. Furthermore, the frequency independence of χ_M'' for **2** contrasts with that of **1**, which showed a slight degree of frequency dependence.²⁴ Likely, this effect results from simplification of metal–organic radical interactions, and possibly an alleviation of spin frustration, following complete chemical reduction of the bridging ligands.⁴²

The observation of magnetic order at 105 K places **2** in a small group of metal–organic solids that display magnetic order above 100 K. All previously reported materials use organonitrile ligands as linkers between metals, the most highly studied of these examples being TCNE (tetracyanoethylene)^{17,43} and TCNQ (tetracyanoquinodimethane).^{13,44,45} Among structurally characterized materials, **2** is only eclipsed by two TCNE-bridged Mn^{II} solids, $Mn^{II}[TCNE]_{3/2}(I_3)_{1/2} \cdot 0.5$ THF and $Mn^{II}[TCNE]I(OH)_2$, each of which is a ferrimagnet below 171 K.^{14,15}

Electrical Conductivity. Bulk magnetic ordering in these compounds is accompanied by electrical conductivity, a rare occurrence in metal–organic materials. Conductivity measurements were performed on pressed pellets of **1**, **1a**, **2**, and **3** using two-probe dc current–voltage techniques (see Figures 8

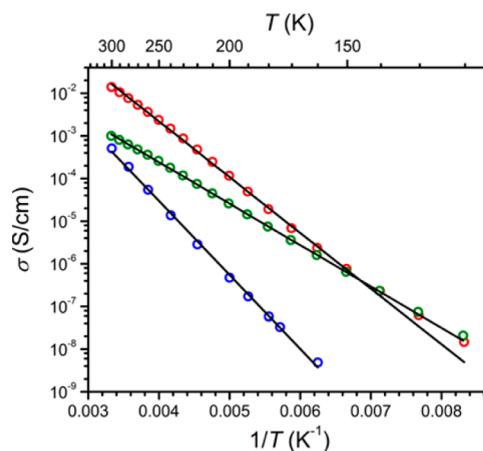


Figure 8. Variable-temperature electrical conductivity data for **1** (red), **1a** (green), and **2** (blue), collected for pressed pellets using two-probe current–voltage techniques. The black lines correspond to Arrhenius fits of the data.

and S12). For **1**, an ambient temperature conductivity of $\sigma = 1.4(7) \times 10^{-2}$ S/cm was measured. Desolvation of **1** to form **1a** resulted in a decrease to $\sigma = 1.0(3) \times 10^{-3}$ S/cm at ambient temperature. This small decrease is likely attributable to the slight structural distortion of the honeycomb network following desolvation,²⁴ which results in a decrease in overlap between metal- and ligand-based orbitals. Indeed, a similar structural distortion and corresponding decrease in conductivity has been observed in topologically similar MOFs.⁴⁶

Chemical reduction to **2** causes a slight reduction in the conductivity to $\sigma = 5.1(3) \times 10^{-4}$ S/cm at ambient temperature. This decrease likely stems from transitioning from incomplete ligand reduction in **1**, which enables ligand mixed-valency and high charge mobility by facile charge hopping, to removal of mixed valency in **2**. The decrease in conductivity may seem at odds with the formal addition of a high-energy electron into the system, but has been previously observed in a three-dimensional iron-quinoid MOF.²⁵ Finally, an ambient temperature conductivity of $\sigma = 1.5(3) \times 10^{-9}$ S/cm was measured for **3** (see Figure S13). This considerably lower value in comparison to the Fe congeners likely stems from the presence of fully occupied Zn^{II} -based d orbitals in **3**, which may hinder charge hopping across the 2D layers.

It is important to note that the observed pressed-pellet conductivity values for low-dimensional materials are often artificially low.^{47–49} These low values can stem from large anisotropy in the conducting pathway, which leads to unfavorable grain boundary interactions. Single-crystal measurements of these materials may reveal conductivity values that are several orders of magnitude higher than those observed in the bulk pellet.

To further probe the nature of the observed conductivity, variable-temperature conductivity data were collected in the temperature range 300–120 K for **1** and **1a** and 300–160 K for **2**. In these temperature regimes, all three compounds display a

linear relationship between the logarithm of conductivity and the inverse of temperature, as expected for thermally activated transport. Corresponding Arrhenius fits to the data between 300 and 160 K provide activation energies of $E_a = 0.26(1)$, $0.19(1)$, and $0.34(1)$ eV for **1**, **1a**, and **2**, respectively. The increase in E_a upon moving from **1** to **2** is in accordance with the lower observed conductivity and supports the removal of a facile charge hopping pathway upon reduction.

The ambient temperature conductivities observed for **1**, **1a**, and **2** represent some of the highest values that have been observed for MOFs.¹² Furthermore, to the best of our knowledge, **1a** displays the highest conductivity yet reported for a material surpassing the symbolic BET surface area of 1000 m²/g. Among permanently porous MOFs with higher conductivity values, the largest reported surface area corresponds to the 2D solid Ni₂(HITP)₃ (HITP = hexaiminotriphenylene), which features a BET surface area of 629 m²/g and an ambient-temperature conductivity of $\sigma = 40$ S/cm.^{18,19}

Literature Context of Magnetism and Conductivity.

Whereas the conductivity and magnetism uncovered for **1**, **1a**, and **2** are remarkable among MOFs when treated separately, their simultaneous coexistence in a single material is nearly unprecedented. A summary of literature reports of structurally characterized materials that exhibit both high-temperature magnetic ordering and high conductivity is enumerated in Figure 9 and Table S1. The majority of these materials have

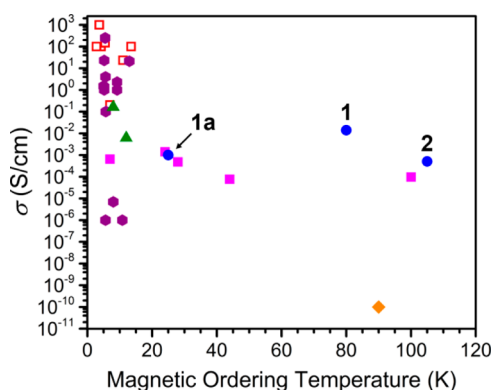


Figure 9. Plot depicting literature examples of structurally characterized metal–organic compounds for which both magnetic ordering and ambient temperature electrical conductivity values have been reported. Blue circles = this work; purple hexagons = metal-oxalate solids cocrystallized with conductive cations;^{7,51} magenta squares = TCNQ-bridged solids;^{13,44} green triangles = 3D iron-quinoid solids;²⁵ orange diamonds = TCNE-bridged solids;⁵³ hollow red squares = halogen-bonded salts.⁵⁰ A full list of these compounds and corresponding values is provided in Table S1.

been optimized for either high-temperature magnetic ordering or high conductivity, but rarely for both. As noted above, in an attempt to optimize both of these two properties, some researchers have synthesized hybrid materials that typically involve inclusion of a conductive guest molecule into a magnetic framework.^{7,11,51} In general, this approach has provided materials with high conductivity but low magnetic ordering temperatures (purple hexagons in Figure 9).

Among metal–organic materials with reported intrinsic conductivity and magnetic order, only organonitrile-containing solids have proven successful in the maximization of both properties. The most notable example is the amorphous material V[TCNE]_x, which can order at temperatures as high as

400 K and can display ambient-temperature conductivity values up to 10^{−3} S/cm.^{17,52} Nevertheless, this conductivity does not appear to transfer to other TCNE-bridged materials, as evidenced by the insulating ($\sigma \leq 10^{-10}$ S/cm) nature of the 2D magnet [Fe^{II}(TCNE)(MeCN)₂][Fe^{III}Cl₄] (orange diamond in Figure 9).⁵³ Among structurally characterized materials, the TCNQ-family displays both high magnetic ordering and conductivity (pink squares in Figure 9). Within this group, a 3D network composed of Ru₂ units bridged by TCNQ-based radical ligands provides the most notable example. This material exhibits a peak in the variable temperature in-phase (χ_M') ac magnetic susceptibility plot at 100 K and a room temperature conductivity of 9.7×10^{-5} S/cm, comparable to the values obtained for **2**.¹³ In sum, compounds **1** and **2** are exceptional in that they simultaneously feature high magnetic ordering temperatures and electrical conductivity, and their porous crystalline structures enable postsynthetic redox reactions. Moreover, the vast scope of chemical tunability possible for benzoquinoid ligands highlights the tremendous potential for metal-quinoid solids to emerge as an important class of conductive magnets.

CONCLUDING REMARKS

The foregoing results demonstrate the ability of metal-quinoid solids to simultaneously exhibit high magnetic ordering temperatures and electrical conductivity. The compound (Me₂NH₂)₂[Fe₂L₃]·2H₂O·6DMF, which features formally 2:1 L^{3−}:L^{2−•}, undergoes magnetic ordering below 80 K and exhibits an electrical conductivity up to $\sigma = 1.4(7) \times 10^{-2}$ S/cm ($E_a = 0.26(1)$ cm^{−1}). By virtue of its porous crystalline structure, the compound can be postsynthetically reduced to give a corresponding framework with exclusively L^{3−•} bridging ligands. This reduced compound shows an increase in magnetic ordering to 105 K and an open hysteresis loop at 100 K, owing to the presence of stronger magnetic exchange interactions, in addition to conductivity up to $\sigma = 5.1(3) \times 10^{-4}$ S/cm ($E_a = 0.34(1)$ cm^{−1}). Current work is geared toward incorporation of related bridging ligands, including those with different ligand substituents and more diffuse donor atoms, in an effort to isolate MOFs that feature higher values of magnetic ordering temperature and electrical conductivity.

ASSOCIATED CONTENT

Supporting Information

The Supporting Information is available free of charge on the ACS Publications website at DOI: 10.1021/jacs.7b00705.

Additional experimental details and characterization data for **1**, **1a**, **2**, and **3** (PDF)
Crystal data for **2** (CIF)

AUTHOR INFORMATION

Corresponding Author

*dharris@northwestern.edu

ORCID

Lei Sun: 0000-0001-8467-6750

Mircea Dincă: 0000-0002-1262-1264

T. David Harris: 0000-0003-4144-900X

Notes

The authors declare no competing financial interest.

■ ACKNOWLEDGMENTS

Work in the Harris lab (J.A.D., I.R.J., and T.D.H.) was supported by the National Science Foundation through Grant DMR-1351959 and Northwestern University. T.D.H. thanks the Alfred P. Sloan Foundation. Work in the Dincă lab (L.S. and M.D.) was supported as part of the Center for Excitronics, an Energy Frontier Research Center funded by the US Department of Energy, Office of Science, Office of Basic Energy Sciences, under award no. DE-SC0001088 (MIT). M.D. gratefully acknowledges early career support from the Sloan Foundation, the Research Corporation for Science Advancement (Cottrell Scholar), and the Dreyfus Foundation. Purchase of the SQUID magnetometer was supported in part by the International Institute of Nanotechnology. Use of the Advanced Photon Source at Argonne National Laboratory was supported by the U.S. Department of Energy, Office of Science, Office of Basic Energy Sciences, under Contract No. DE-AC02-06CH11357. The X-ray crystallography made use of the Integrated Molecular Structure Education and Research Center (IMSERC) at Northwestern University, with support from the Soft and Hybrid Nanotechnology Experimental (SHyNE) Resource (NSF NNCI-1542205), the State of Illinois, and International Institute for Nanotechnology (IIN). Raman spectroscopy was performed at the SPID facility of Northwestern University's NUANCE Center, with support from the Soft and Hybrid Nanotechnology Experimental (SHyNE) Resource (NSF ECCS-1542205); the MRSEC program (NSF DMR-1121262) at the Materials Research Center; the International Institute for Nanotechnology (IIN); the Keck Foundation; and the State of Illinois, through the IIN. Metals analysis was performed at the Northwestern University Quantitative Bioelement Imaging Center. We thank Dr. C. D. Malliakas, Ms. Y. Wang, and Mr. A. Banisafar for experimental assistance.

■ REFERENCES

- (1) (a) Prigodin, V. N.; Raju, N. P.; Pokhodnya, K. I.; Miller, J. S.; Epstein, A. J. *Adv. Mater.* **2002**, *14*, 1230. (b) Rao, C. N. R.; Cheetham, A. K.; Thirumurugan, A. J. *Phys.: Condens. Matter* **2008**, *20*, 083202.
- (2) (a) Kurmoo, M. *Chem. Soc. Rev.* **2009**, *38*, 1353. (b) Dechambe-noit, P.; Long, J. R. *Chem. Soc. Rev.* **2011**, *40*, 3249. (c) Maspocho, D.; Ruiz-Molina, D.; Veciana, J. J. *Mater. Chem.* **2004**, *14*, 2713.
- (3) (a) Sanvito, S. *Chem. Soc. Rev.* **2011**, *40*, 3336. (b) Awschalom, D. D.; Flatté, M. E. *Nat. Phys.* **2007**, *3*, 153. (c) Yoo, J.-W.; Chen, C.-Y.; Jang, H. W.; Bark, C. W.; Prigodin, V. N.; Eom, C. B.; Epstein, A. J. *Nat. Mater.* **2010**, *9*, 638.
- (4) (a) Žutić, I.; Fabian, J.; Das Sarma, S. *Rev. Mod. Phys.* **2004**, *76*, 323. (b) Fert, A. *Thin Solid Films* **2008**, *517*, 2.
- (5) Yaghi, O. M.; Li, G.; Li, H. *Nature* **1995**, *378*, 703.
- (6) (a) Yaghi, O. M.; O'Keeffe, M.; Ockwig, N. W.; Chae, H. K.; Eddaoudi, M.; Kim, J. *Nature* **2003**, *423*, 705. (b) Furukawa, H.; Cordova, K. E.; O'Keeffe, M.; Yaghi, O. M. *Science* **2013**, *341*, 974.
- (7) Coronado, E.; Galán-Mascarós, J. R.; Gómez-García, C. J.; Laukhin, V. *Nature* **2000**, *408*, 447.
- (8) (a) Kaye, S. S.; Choi, H. J.; Long, J. R. *J. Am. Chem. Soc.* **2008**, *130*, 16921. (b) Kobayashi, Y.; Jacobs, B.; Allendorf, M. D.; Long, J. R. *Chem. Mater.* **2010**, *22*, 4120. (c) Talin, A. A.; Centrone, A.; Ford, A. C.; Foster, M. E.; Stavila, V.; Haney, P.; Kinney, R. A.; Szalai, V.; Grabaly, F. E.; Yoon, H. P.; Léonard, F.; Allendorf, M. D. *Science* **2014**, *343*, 66.
- (9) Choi, H. J.; Suh, M. P. *J. Am. Chem. Soc.* **2004**, *126*, 15844.
- (10) (a) Hoskins, B. F.; Robson, R. *J. Am. Chem. Soc.* **1990**, *112*, 1546. (b) Seo, J. S.; Whang, D.; Lee, H.; Jun, S. I.; Oh, J.; Jeon, Y. J.; Kim, K. *Nature* **2000**, *404*, 982. (c) Wang, Z.; Cohen, S. M. *Chem. Soc. Rev.* **2009**, *38*, 1315. (d) Chui, S. S.-Y.; Lo, S. M.-F.; Charmant, J. P. H.; Orpen, A. G.; Williams, I. D. *Science* **1999**, *283*, 1148.
- (11) Zeng, M.-H.; Yin, Z.; Tan, Y.-X.; Zhang, W.-X.; He, Y.-P.; Kurmoo, M. *J. Am. Chem. Soc.* **2014**, *136*, 468.
- (12) Sun, L.; Campbell, M. G.; Dincă, M. *Angew. Chem., Int. Ed.* **2016**, *55*, 3566.
- (13) Motokawa, N.; Miyasaka, H.; Yamashita, M.; Dunbar, K. R. *Angew. Chem., Int. Ed.* **2008**, *47*, 7760.
- (14) Stone, K. H.; Stephens, P. W.; McConnell, A. C.; Shurdha, E.; Pokhodnya, K. I.; Miller, J. S. *Adv. Mater.* **2010**, *22*, 2514.
- (15) Lapidus, S. H.; McConnell, A. C.; Stephens, P. W.; Miller, J. S. *Chem. Commun.* **2011**, *47*, 7602.
- (16) (a) Caneschi, A.; Gatteschi, D.; Sessoli, R.; Rey, P. *Acc. Chem. Res.* **1989**, *22*, 392. (b) Vostrikova, K. E. *Coord. Chem. Rev.* **2008**, *252*, 1409. (c) Faust, T. B.; D'Alessandro, D. *RSC Adv.* **2014**, *4*, 17498.
- (17) Manriquez, J. M.; Yee, G. T.; McLean, R. S.; Epstein, A. J.; Miller, J. S. *Science* **1991**, *252*, 1415.
- (18) Sheberla, D.; Sun, L.; Blood-Forsythe, M. A.; Er, S.; Wade, C. R.; Brozek, C. K.; Aspuru-Guzik, A.; Dincă, M. *J. Am. Chem. Soc.* **2014**, *136*, 8859.
- (19) Miner, E. M.; Fukushima, T.; Sheberla, D.; Sun, L.; Surendranath, Y.; Dincă, M. *Nat. Commun.* **2016**, *7*, 10942.
- (20) (a) Kitagawa, S.; Kawata, S. *Coord. Chem. Rev.* **2002**, *224*, 11 and references therein. (b) Abrahams, B. F.; Coleiro, J.; Ha, K.; Hoskins, B. F.; Orchard, S. D.; Robson, R. *J. Chem. Soc., Dalton Trans.* **2002**, 1586 and references therein.
- (21) (a) Luo, T.-T.; Liu, Y.-H.; Tsai, H.-L.; Su, C.-C.; Ueng, C.-H.; Lu, K.-L. *Eur. J. Inorg. Chem.* **2004**, *2004*, 4353. (b) Abrahams, B. F.; Hudson, T. A.; McCormick, L. J.; Robson, R. *Cryst. Growth Des.* **2011**, *11*, 2717. (c) Atzori, M.; Benmansour, S.; Espallargas, G. M.; Clemente-León, M.; Abhervé, A.; Gómez-Claramunt, P.; Coronado, E.; Artizzu, F.; Sessini, E.; Deplano, P.; Serpe, A.; Mercuri, M. L.; García, C. J. *Inorg. Chem.* **2013**, *52*, 10081. (d) Kingsburg, C. J.; Abrahams, B. F.; D'Alessandro, D. M.; Hudson, T. A.; Murase, R.; Robson, R.; White, K. F. *Cryst. Growth Des.* [online early access]. 2017, DOI: 10.1021/acs.cgd.6b01886
- (22) (a) Rodriguez, J. H.; Wheeler, D. E.; McCusker, J. K. *J. Am. Chem. Soc.* **1998**, *120*, 12051. (b) Guo, D.; McCusker, J. K. *Inorg. Chem.* **2007**, *46*, 3257. (c) Schrauben, J. N.; Guo, D.; McCracken, J. L.; McCusker, J. K. *Inorg. Chim. Acta* **2008**, *361*, 2539.
- (23) (a) Dei, A.; Gatteschi, D.; Pardi, L.; Russo, U. *Inorg. Chem.* **1991**, *30*, 2589. (b) Heinze, K.; Huttner, G.; Zsolnai, L.; Jacobi, A.; Schöber, P. *Chem. - Eur. J.* **1997**, *3*, 732. (c) Min, K. S.; Rheingold, A. L.; DiPasquale, A. G.; Miller, J. S. *Inorg. Chem.* **2006**, *45*, 6135. (d) Min, K. S.; DiPasquale, A. G.; Golen, J. A.; Rheingold, A. L.; Miller, J. S. *J. Am. Chem. Soc.* **2007**, *129*, 2360. (e) Guo, D.; McCusker, J. K. *Inorg. Chem.* **2007**, *46*, 3257. (f) Jeon, I.-R.; Park, J. G.; Xiao, D. J.; Harris, T. D. *J. Am. Chem. Soc.* **2013**, *135*, 16845. (g) DeGayner, J. A.; Jeon, I.-R.; Harris, T. D. *Chem. Sci.* **2015**, *6*, 6639.
- (24) Jeon, I. R.; Negru, B.; Van Duyne, R. P.; Harris, T. D. *J. Am. Chem. Soc.* **2015**, *137*, 15699.
- (25) Durago, L. E.; Aubrey, M. L.; Yu, C. J.; Gonzalez, M. I.; Long, J. R. *J. Am. Chem. Soc.* **2015**, *137*, 15703.
- (26) Halis, S.; Inge, A. K.; Dehning, N.; Weyrich, T.; Reinsch, H.; Stock, N. *Inorg. Chem.* **2016**, *55*, 7425.
- (27) APEX2, v. 2009; Bruker Analytical X-ray Systems, Inc.: Madison, WI, 2009.
- (28) Sheldrick, G. M. SADABS, version 2.03, Bruker Analytical X-ray Systems, Inc.: Madison, WI, 2000.
- (29) Sheldrick, G. M. SHELXTL, version 6.12; Bruker Analytical X-ray Systems, Inc.: Madison, WI, 2000.
- (30) Dolomanov, O. V.; Bourhis, L. J.; Gildea, R. J.; Howard, J. A.; Puschmann, H. *J. Appl. Crystallogr.* **2009**, *42*, 339.
- (31) Bain, G. A.; Berry, J. F. *J. Chem. Educ.* **2008**, *85*, 532.
- (32) Wudl, F.; Bryce, M. R. *J. Chem. Educ.* **1990**, *67*, 717.
- (33) Ma, L.; Jin, A.; Xie, Z.; Lin, W. *Angew. Chem., Int. Ed.* **2009**, *48*, 9905.
- (34) (a) Choi, H. J.; Suh, M. P. *J. Am. Chem. Soc.* **2004**, *126*, 15844. (b) Meilikhov, M.; Yusenko, K.; Torrisi, A.; Jee, B.; Mellot-Draznieks,

- C.; Pöppl, A.; Fischer, R. A. *Angew. Chem., Int. Ed.* **2010**, *49*, 6212.
- (c) Huang, C.; Wu, J.; Song, C.; Ding, R.; Qiao, Y.; Hou, H.; Chang, J.; Fan, Y. *Chem. Commun.* **2015**, *51*, 10353. (d) Gui, B.; Meng, X.; Chen, Y.; Tian, J.; Liu, G.; Shen, C.; Zeller, M.; Yuan, D.; Wang, C. *Chem. Mater.* **2015**, *27*, 6426.
- (35) (a) Neumeyer, J. L.; Cannon, J. G. *J. Org. Chem.* **1961**, *26*, 4681. (b) Zhang, J.; Chen, S.; Nieto, R. A.; Wu, T.; Feng, P.; Bu, X. *Angew. Chem., Int. Ed.* **2010**, *49*, 1267. (c) Johnson, J. A.; Chen, S.; Reeson, T. C.; Chen, Y.-S.; Zeng, X. C.; Zhang, J. *Chem. - Eur. J.* **2014**, *20*, 7632.
- (36) Nagayoshi, K.; Kabir, M. K.; Tobita, H.; Honda, K.; Kawahara, M.; Katada, M.; Adachi, K.; Nishikawa, H.; Ikemoto, I.; Kumagai, H.; Hosokoshi, Y.; Inoue, K.; Kitagawa, H.; Kawata, S. *J. Am. Chem. Soc.* **2003**, *125*, 221.
- (37) Baum, A. E.; Lindeman, S. V.; Fiedler, A. T. *Chem. Commun.* **2013**, *49*, 6531.
- (38) Hartl, F.; Stufkens, D. J.; Vlček, A. *Inorg. Chem.* **1992**, *9*, 1687.
- (39) Holt, B. T. O.; Vance, M. A.; Mirica, L. M.; Heppner, D. E.; Stack, T. D. P.; Solomon, E. I. *J. Am. Chem. Soc.* **2009**, *131*, 6421.
- (40) (a) Buschmann, W. E.; Ensling, J.; Gütlich, P.; Miller, J. S. *Chem. - Eur. J.* **1999**, *5*, 3019. (b) Viertelhaus, M.; Adler, P.; Clérac, R.; Anson, C. E.; Powell, A. K. *Eur. J. Inorg. Chem.* **2005**, *2005*, 692.
- (41) Buchanan, R. M.; Kessel, S. L.; Downs, H. H.; Pierpont, C. G.; Hendrickson, D. N. *J. Am. Chem. Soc.* **1978**, *100*, 7894.
- (42) Mydosh, J. A. *Spin Glasses*; Taylor & Francis: London, 1993.
- (43) (a) Zhang, J.; Engsling, J.; Ksenofontov, P. G.; Epstein, A. J.; Miller, J. S. *Angew. Chem., Int. Ed.* **1998**, *37*, 657. (b) Gîrțu, M. A.; Wynn, C. M.; Zhang, J.; Miller, J. S.; Epstein, A. J. *Phys. Rev. B: Condens. Matter Mater. Phys.* **2000**, *61*, 492. (c) Fitzgerald, J. P.; Kaul, B. B.; Yee, G. T. *Chem. Commun.* **2000**, *49*. (d) Vickers, E. B.; Selby, T. D.; Miller, J. S. *J. Am. Chem. Soc.* **2004**, *126*, 3716. (e) Pokhodnya, K. I.; Bonner, M.; Her, J.-H.; Stephens, P. W.; Miller, J. S. *J. Am. Chem. Soc.* **2006**, *128*, 15592.
- (44) Clérac, R.; O’Kane, S.; Cowen, J.; Ouyang, X.; Heintz, R.; Zhao, H.; Bazile, M. J.; Dunbar, K. R. *Chem. Mater.* **2003**, *15*, 1840.
- (45) Motokawa, N.; Matsunaga, S.; Takaishi, S.; Miyasaka, H.; Yamashita, M.; Dunbar, K. R. *J. Am. Chem. Soc.* **2010**, *132*, 11943.
- (46) Sun, L.; Hendon, C. H.; Minier, M. A.; Walsh, A.; Dincă, M. *J. Am. Chem. Soc.* **2015**, *137*, 6164.
- (47) Givaja, G.; Amo-Ochoa, P.; Gómez-García, C. J.; Zamora, F. *Chem. Soc. Rev.* **2012**, *41*, 115.
- (48) Jeon, I.-R.; Sun, L.; Negru, B.; Van Duyne, R. P.; Dincă, M.; Harris, T. D. *J. Am. Chem. Soc.* **2016**, *138*, 6583.
- (49) Sun, L.; Park, S. S.; Sheberla, D.; Dincă, M. *J. Am. Chem. Soc.* **2016**, *138*, 14772.
- (50) (a) Coronado, E.; Galán-Mascarós, J. R. *J. Mater. Chem.* **2005**, *15*, 66. (b) Alberola, A. E.; Coronado, E.; Galán-Mascarós, J. R.; Giménez-Saiz, C.; Gómez-García, C. J.; Martínez-Ferrero, E.; Murcia-Martínez, A. *Synth. Met.* **2003**, *135–136*, 687.
- (51) (a) Miyasaka, A.; Yamazaki, H.; Aimatsu, M.; Enoki, T.; Watanabe, R.; Ogura, E.; Kuwatani, Y.; Iyoda, M. *Inorg. Chem.* **2007**, *46*, 3353. (b) Nishijo, J.; Ogura, E.; Yamaura, J.; Miyazaki, A.; Enoki, T.; Takano, T.; Kuwatani, Y.; Iyoda, M. *Synth. Met.* **2003**, *133–134*, 539. (c) Nishijo, J.; Miyazaki, A.; Enoki, T. *Inorg. Chem.* **2005**, *44*, 2393. (d) Enomoto, K.; Yamaura, J.-I.; Miyazaki, A.; Enoki, T. *Bull. Chem. Soc. Jpn.* **2003**, *76*, 945. (e) Enomoto, K.; Miyazaki, A.; Enoki, T. *Synth. Met.* **2003**, *135*, 561. (f) Fujiwara, E.; Yamamoto, K.; Shimamura, M.; Zhou, B.; Kobayashi, A.; Takahashi, K.; Okano, Y.; Cui, H.; Kobayashi, H. *Chem. Mater.* **2007**, *19*, 553.
- (52) Du, G.; Joo, J.; Epstein, A. J.; Miller, J. S. *J. Appl. Phys.* **1993**, *73*, 6566.
- (53) Shum, W. W.; Epstein, A. J.; Miller, J. S. *Phys. Rev. B: Condens. Matter Mater. Phys.* **2009**, *80*, 064403.